



Optical Diagnostics in a High-Pressure Combustor with Gaseous Oxygen and Kerosene

Henry C. Balance,* Oleksandr Bibik,[†] and Timothy S. Cook[‡]

Georgia Institute of Technology, Atlanta, Georgia 30332

Stephen Danczyk[§] and S. Alexander Schumaker[¶]

U.S. Air Force Research Laboratory, Edwards Air Force Base, California 93524

and

Vigor Yang^{**} and Timothy C. Lieuwen^{††}

Georgia Institute of Technology, Atlanta, Georgia 30332

DOI: 10.2514/1.B37050

This paper presents analysis of results from optical diagnostics in a high-pressure combustor burning gaseous oxygen (GOX) and liquid kerosene RP-2 fuel through a jet-swirl coflow injector. The objectives of the experiment were to measure flame stabilization and position under high-pressure conditions. Data were obtained at pressures from 2 to 16.5 MPa and mixture ratios from 2.9 to 20. High-speed cameras captured side-on chemiluminescence and infrared images of the flame. Results show that the flame-spreading angle from the injector ranges from approximately 3 to 6 deg, varying with pressure and propellant mass flow rate. A novel borescope was used to image the flame from upstream of the GOX post, enabling visualization of the flame near its stabilization location. The flame stabilization characteristics change significantly with the fuel flow velocity (which is proportional to pressure). At low pressures and fuel flow velocities, the flame appears to be distributed azimuthally in a nearly axisymmetric manner. At higher velocities, helical spirals of luminosity develop near the GOX post. In addition, the side-on views reveal concentrated streaks of, presumably, fuel entering the combustion chamber. These results suggest that computations must resolve the individual fuel injection orifices, to capture the flame stabilization.

Nomenclature

G_1	=	test article, including injector, combustor, and nozzle sections
P	=	pressure in the main chamber, MPa
P'	=	rms value of fluctuating pressure in the main chamber, kPa
PC1	=	static pressure from G_1 main chamber pressure sensor (location 18.67 cm downstream of injector face), MPa
PC2	=	static pressure from G_1 main chamber pressure sensor (location 28.83 cm downstream of injector face), MPa
$T_{GOXInlet}$	=	gaseous oxygen temperature at inlet to the injector
$T_{GOXPostTC}$	=	averaged perimeter metal temperature of the injector gaseous oxygen post tip thermocouple
T_{LHC}	=	temperature of the liquid hydrocarbon fuel entering the injector
v_{LHC}	=	reference fuel exit velocity
α	=	dimensionless gaseous oxygen post temperature
a_{avg}	=	time average of α during data window

I. Introduction

THERMOACOUSTIC instabilities have plagued the development of liquid propellant rocket engines for decades [1,2]. These combustion instabilities are caused by the coupling between hydrodynamics, combustion processes, and chamber acoustics [3]. They can produce severe vibration and high heat transfer rate, which may lead to catastrophic failure of the combustion system. Understanding the physiochemical mechanisms for these instabilities, particularly how the flame responds to flow disturbances, is a critical item for predicting their occurrence. Such knowledge, however, is limited, due to difficulties in viewing and measuring the underlying processes in the very high-pressure and high-temperature rocket environment. Two key inputs, flame stabilization and propellant mixing and distribution mechanisms, are needed to understand the dynamic response of flames to disturbances [4,5].

Subscale single and multi-injector experimental combustors have been employed since the 1950s to economically investigate thermoacoustic combustion instabilities. With the development of laser-based optical diagnostics in the 1960s, providing optical access to these experimental combustors at high pressures became a significant engineering challenge. Santoro carried out Raman spectroscopy for H_2 , O_2 , and H_2O species measurements in GOX/ GH_2 combustion experiments at pressures up to 6.9 MPa [6,7]; significant effort was expended to develop windows to withstand the high-power lasers required for Raman diagnostics and for the extreme combustion chamber conditions. At much lower pressures (i.e., $p < 1.4$ MPa), OH planar laser-induced fluorescence, laser-induced incandescence, two-component PDPA, and two-component LDV were all employed.

Similarly, Smith et al. have conducted experiments on LOX/ LH_2 propellants in an optically accessible facility designed to operate up to 10 MPa [8]. The article was optically accessible through three windows immediately downstream of the injector plane, allowing high-speed cameras to capture spontaneous OH* chemiluminescence, H_2O emissions, and shadowgraph images. Klimenko et al. later applied coherent anti-Stokes Raman spectroscopy to this facility to map temperature within the combustor [9]. Following the LOX/ LH_2 research, a multi-injector experimental facility with transverse forcing was developed, using high-speed OH* and CH* chemiluminescence and schlieren diagnostics at chamber operating

Received 9 January 2018; revision received 28 April 2018; accepted for publication 3 August 2018; published online 26 October 2018. Copyright © 2018 by Timothy C. Lieuwen. Published by the American Institute of Aeronautics and Astronautics, Inc., with permission. All requests for copying and permission to reprint should be submitted to CCC at www.copyright.com; employ the ISSN 0748-4658 (print) or 1533-3876 (online) to initiate your request. See also AIAA Rights and Permissions www.aiaa.org/randp.

*Research Engineer, Aerospace Engineering, 635 Strong Street.

[†]Research Scientist, Aerospace Engineering, 635 Strong Street.

[‡]Graduate Student, Aerospace Engineering, 635 Strong Street. Student Member AIAA.

[§]Research Scientist, AFRL/RQRC, 10 Saturn Blvd.

[¶]Research Engineer, AFRL/RQRC, 10 E. Saturn Blvd, Building 8451. Senior Member AIAA.

**William R. T. Oakes Professor and Chair, School of Aerospace Engineering, 313 Montgomery Knight Building. Fellow AIAA.

^{††}David S. Lewis, Jr. Professor, Aerospace Engineering, 270 Ferst Drive. Fellow AIAA.

pressures up to 6 MPa [10]. Such operating pressures are also typical of the experiments conducted on the multi-injector transverse-forced multi-injector combustor (MIC) and follow-on very high amplitude modulator (VHAM) combustors [11,12]. These facilities also use OH* and CH* imaging to characterize the unsteady flame response.

The continuously variable resonance combustor used a gas-centered swirl-coaxial injector with a variable length oxidizer post in the injector, allowing for tunable resonant responses [13]. This rig evolved into the discretely variable resonance combustor, with an updated injector mechanism [14]. Both of these rigs operate at pressures up to 4.1 MPa, with either CH₄ or liquid hydrocarbon fuels. Fiber optics and sapphire lenses are used in both of these test articles to measure CH* and OH* emissions. A viewing window is incorporated into the transverse instability combustor facility, although this facility is limited to pressures of 1.4 MPa [15].

In addition to the structural challenges of developing systems capable of withstanding the pressures and temperatures of interest,

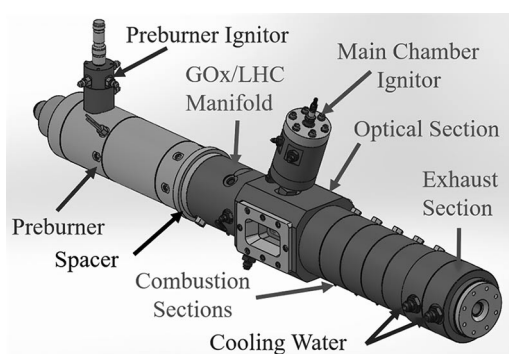


Fig. 1 Test article and preburner arrangement.

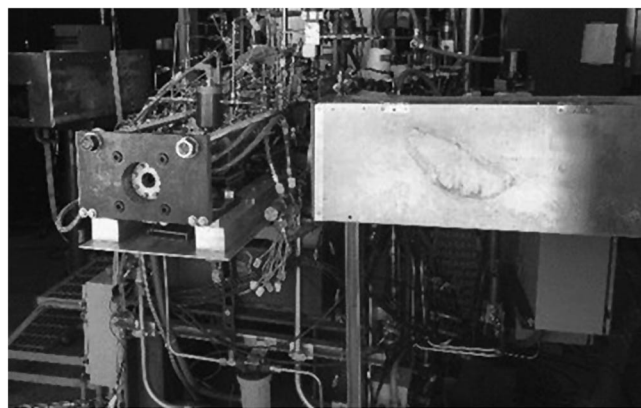


Fig. 2 Test article installation in test cell.

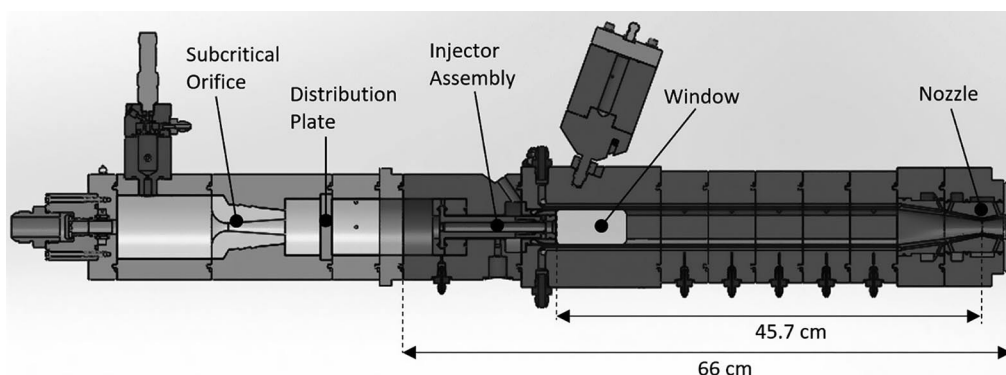


Fig. 3 Cross section of G1 test article and preburner assembly.

liquid hydrocarbon propellants present further complications to optical diagnostics, in the form of soot formation in locally rich regions of combustion. The soot and unevaporated fuel surrounding the flame strongly absorb visible wavelength emissions. Subscale rocket combustor experiments conducted by Roa et al. have revealed the presence of both a soot cloud that swirls about the injector and a liquid fuel sheet emanating from the injector and obscuring the field for optical diagnostics [16]. That work used RP-2 as fuel, and the diagnostics were based on chemiluminescence and schlieren techniques.

Although soot is opaque to visible and ultraviolet light, it is to some extent transmissive in the midwave infrared spectrum. Thus, it is possible to measure the thermal emissions of species such as CO₂ and H₂O that emit in this spectrum in environments that prohibit the use of other optical diagnostics. Infrared emissions from ambient pressure flames have been compared to computational models [17]. Significant uncertainty exists, however, as to the utility of infrared emission measurements in liquid fueled environments at rocket operating pressures.

This paper presents the methodology and results from visible and infrared diagnostics in a high-pressure combustor with gaseous oxygen and liquid kerosene as propellants. The injector of concern has a gas-center, liquid-swirl coflow configuration, similar to those commonly used in the main combustion chamber of an oxidizer-rich, staged combustion cycle engines [18–21]. The visible and infrared emissions from the combustion chamber were studied to evaluate the possibility of identifying heat reaction zones and subsequent evolution of the flames. The most significant result of this work was the acquisition of optical, temperature, and pressure data at pressures up to 16.5 MPa, using both side-on imaging and imaging from a custom borescope integrated with the GOX post.

II. Experimental Facility

The experiments were carried out in the EC-1 test cell at the U.S. Air Force Research Laboratory (AFRL), Edwards Air Force Base. The oxidizer gases, liquid hydrocarbon fuel (LHC), and cooling water were all provided using AFRL's existing experimental infrastructure. RP-2 and heated GOX were used as fuel and oxidizer for all testing. The test article was mounted on the EC-1 test stand and integrated with AFRL's existing GOX/hydrogen gas (GH₂) preburner [22]. Figure 1 shows the experimental facility in the EC-1 test cell. Figure 2 shows a model of the test article, adjoined to the preburner.

The preburner has been used intensively for high-pressure single injector element combustion research. It provides a preheated oxygen-rich flow at an average temperature of 645 ± 2 K directly to the GOX manifold of the G1 test article. The preburner can operate over a wide range of oxidizer-to-fuel mass mixture ratios (MRs) to support G1 combustion chamber mixture ratios between 2.5 and 20. The preburner consists of a spark igniter and a GOX/GH₂ burner. Downstream of the burner is a subcritical nozzle followed by a flow distribution plate, as shown in Fig. 3.

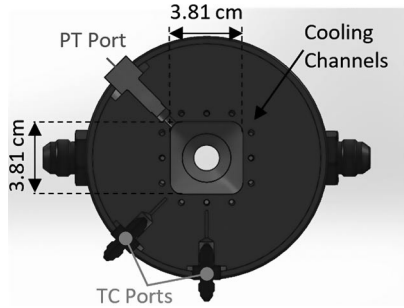


Fig. 4 Transverse cross section of combustion chamber.

The G1 test article consists of the following major components: GOX/LHC manifold, an optically accessible section for flame visualization, a GOX/GH₂ spark igniter, five combustion chamber sections, a transition section, and an exhaust nozzle. Sections downstream of the GOX/LHC manifold are water-cooled. The G1 test article has a length of 66 cm and an internal combustion chamber cross section of 3.81 by 3.81 cm with 0.635-cm-radius corners. The length of the combustion chamber from the injector face to the exhaust nozzle throat is 45.7 cm. The cross section of the combustion chamber is shown in Fig. 4.

Shielded gas-centered swirl-coaxial injectors were fabricated for this testing. Figure 5 shows the longitudinal cross section of the optical section with the injector on the left side, whereas Fig. 6 shows a longitudinal and transverse cross section of the injector geometry. Preheated GOX travels down the central GOX post. Fuel, highlighted in yellow in Figs. 5 and 6, is injected tangentially into the annulus between the GOX post and the injector cup through 10 radially spaced orifices, arranged in two rows of five.

The optical section of the combustion chamber incorporates two 3.81×7.62 cm viewing windows for optical access, one on each side of the tunnel, immediately downstream of the injector face. Quartz and sapphire glass windows were used with both single and double window designs, depending on the diagnostic technique

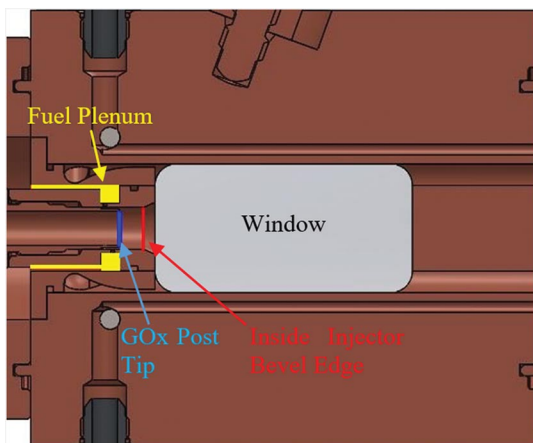


Fig. 5 Cross section of injector and optical section.

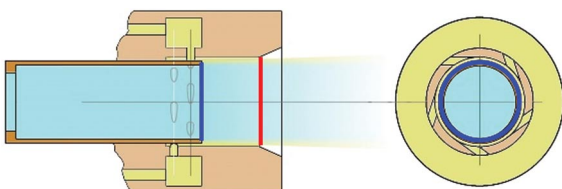


Fig. 6 Cross sections of GOX-centered swirl coaxial injector.

employed. The windows were protected from thermal damage by nitrogen gas curtain flows from vertical slot nozzles on each side of the injector face.

III. Diagnostics

A number of different diagnostic techniques were employed in the present work. The test campaigns and operating conditions are summarized in Appendix A. In the first test campaign, ultraviolet (UV) and visible optical diagnostics were provided by two high-speed, 12 bit, intensified cameras, situated on opposite sides of the combustor, simultaneously recording OH* (308–330 nm) and CH*/CO₂* (420–432 nm) chemiluminescence through the window downstream of the injector face. For the second and third test campaigns, a high-speed, 14 bit, infrared (IR) camera was adopted in place of the UV for comparison between CH*/CO₂* chemiluminescence and infrared H₂O (2.75 μm) or CO₂ (4.5 μm) thermal radiation. The selection between H₂O (2.75 μm) and CO₂ (4.5 μm) bands was provided by two IR band-pass filters mounted on the filter wheel inside of the camera. The center wavelength (CWL) is 2.75 μm, and the full width at half-maximum (FWHM) is 0.5 μm for the 2.75 μm band. The CWL is 4.50 μm, and FWHM is 0.5 μm for the 4.5 μm band. Frame rate for the IR camera was 1700 FPS. A 2.54-cm-thick fused silica window was used for images of 2.75 μm band emission, whereas a sapphire window was used for the 4.5 μm band. The camera safety box was equipped with a 2.54-cm-thick, 10.16-cm-diam, silica window installed on the front panel. These windows were obtained for the third test campaign, which alternated the use of both IR filters, whereas only the 2.75 μm filter was employed during the second test campaign. Figure 7 shows a typical arrangement of the high-speed cameras in relation to the test article.

To determine the relative proximity of the flame to the injector GOX post tip, an integrated injector–thermocouple was fabricated to provide a perimeter-averaged temperature at the tip. This custom thermocouple forms the GOX post, dividing the LHC and GOX for the coaxial injector. An insulator separates the Alumel and Chromel layers in the body of the GOX post, with the sensing element formed only at the tip by a laser weld between the Alumel and Chromel layers, depicted in Fig. 8a. The sensing element is 50 μm thick, giving the thermocouple a response time of less than 40 ms in the injector environment. The tip is located at the point of injection, where the first contact occurs between the fuel and oxidizer. The temperature uncertainty is ± 2 K.

Starting in the second test campaign, a borescope with a CH* (420–432 nm) filtered camera and intensifier was employed to provide optical access into the injector cup. Figure 8a illustrates the design of the borescope within the injector. Using a prism that is mounted into the GOX channel, the borescope captures images from inside the injector, looking downstream into the combustion chamber. The borescope is mounted 42 deg vertically from the injector axis. The bottom of the 22.5 deg prism sits parallel to the injector axis, but recessed 0.25 mm into the GOX post wall,

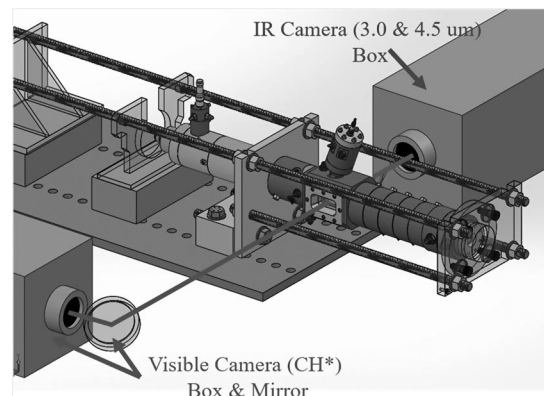
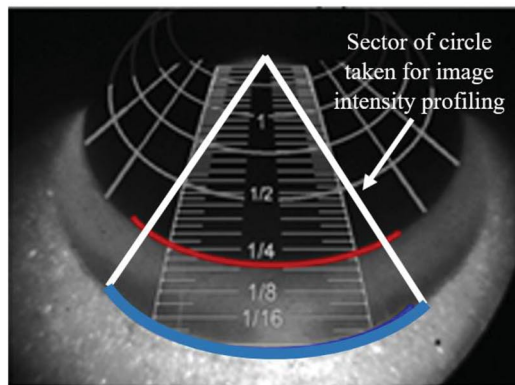
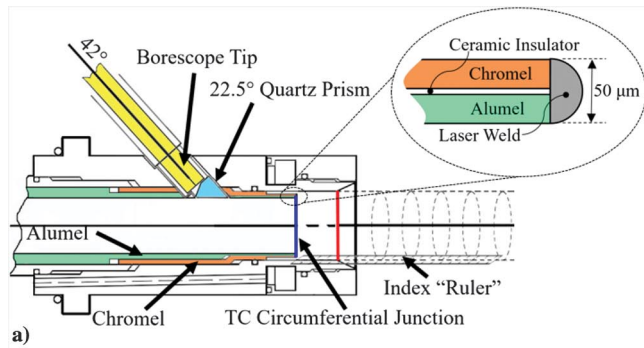
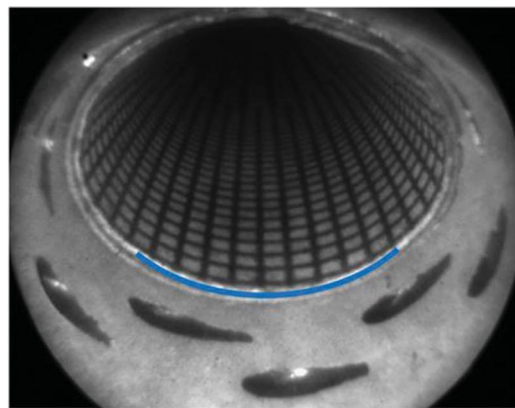


Fig. 7 Test article and high-speed camera arrangement.



b)



c)

Fig. 8 Representations of a) injector head with borescope and GOX post tip thermocouple, b) borescope field of view (ruler measure in inches), and c) borescope calibration image with GOX post removed.

introducing a slight disruption of the GOx flow along the top of the GOx channel. Figure 8b shows the borescope field of view, with an annotated ruler providing a measurement of visual depth from the GOx post tip into the chamber. Note that the ruler measurement in Fig. 8b is in inches. The blue and red lines of Fig. 8b depict the location of the GOx post tip and the inside bevel edge, respectively. The white lines frame the arc sections over which luminosity integration is performed for the analysis of flame structure near the injector cup in the next section. The GOx post, which normally blocks the fuel annulus from the borescope field of view, was removed for the calibration image in Fig. 8c, and the locations of fuel orifices are visible. A 1 mm grid forms a cylinder, of the same diameter as the GOx post, extending into the chamber.

A number of pressure transducers (PTs), both high-frequency (HF, with good frequency response up to 50 kHz) and low-frequency (LF, good frequency response to 500 Hz), measure gas pressures inside the test article. This paper presents data only from the LF sensors for measurement of chamber mean pressure and oscillating pressures due to low-frequency instabilities. Figure 9 provides a

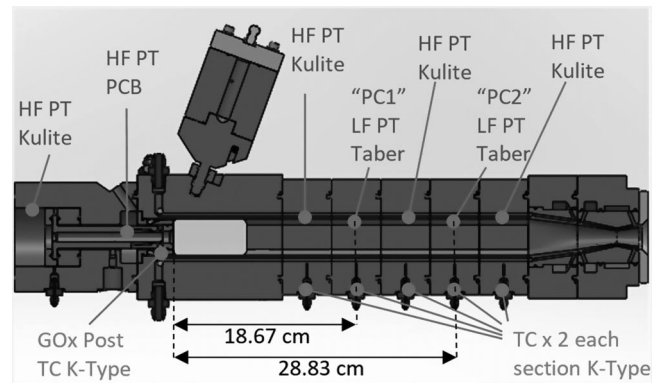


Fig. 9 Test article instrument locations.

diagram of HF and LF sensor locations and axial distance from the injector outlet face to the LF sensors. Chamber pressure sensors are located on the top corner of the chamber cross section, as in Fig. 4. The uncertainty in all low-frequency pressure measurements is 0.15% relative.

Additional facility sensors provide propellant supply pressures, temperatures, and flow rates entering the test article. Gas flow rates are measured using critical flow nozzles with uncertainties less than 0.6% for GOx and less than 10% for nitrogen. LHC flow rate is measured using a cavitating venturi with uncertainty of 0.4–0.5%. LHC flow rate was also measured for certain conditions using a positive displacement spur gear flow meter with an uncertainty of 0.5%. Uncertainties in GOx and LHC flow rates lead to an uncertainty in MR of approximately 1%. The full suite of diagnostics is summarized in Table B1. An overview of facility instrumentation is addressed by Lightfoot et al. [23].

IV. Analysis and Results

The pressure transducers and thermocouples record continuously throughout each test. The test procedure is automated by a timing system, which consecutively triggers the start of the oxidizer flow, fuel flow, ignition, and purge for the rocket. Each successful test achieves sustained combustion for approximately 2.5 s, with an approximately 1 s “data window” of steady-state conditions. The ending purge of the fuel system creates short, often steady, lean mixture-ratio conditions at a lower mean pressure, as nitrogen forces the remaining fuel from the supply system. This secondary data window yields much lower soot and, consequently, clear combustion images, which were used during the third test campaign. Fuel flow rate during this period was measured using the in-line gear-type flow meter, listed in Appendix B.

Equation (1) defines the mixture ratio. The stoichiometric MR value for GOx/RP-2 is 3.42, with greater values indicating lean combustion:

$$MR = \frac{\dot{m}_{O_x}}{\dot{m}_{LHC}} \quad (1)$$

The sensitivity of RP-2 density to pressure at the upstream fuel temperature was calculated. Results indicated that it is essentially constant over the pressure range tested here. The velocity of the fuel exiting the injection orifices is thus directly proportional to pressure at a given MR value. For this reason, we define a reference fuel velocity, in Eq. (2), as the average velocity of fuel exiting the fuel jets, using a density calculated from the upstream reference temperature. A_N denotes the sum of the cross-sectional area of the 10 fuel inlet orifices, shown in Figs. 6 and 8:

$$v_{LHC} = \frac{\dot{m}_{LHC}}{\rho_{LHC} \times A_N} \quad (2)$$

Figures 10 and 11 provide representative time histories at main chamber pressures of 12.4 and 16.5 MPa, respectively. Each figure

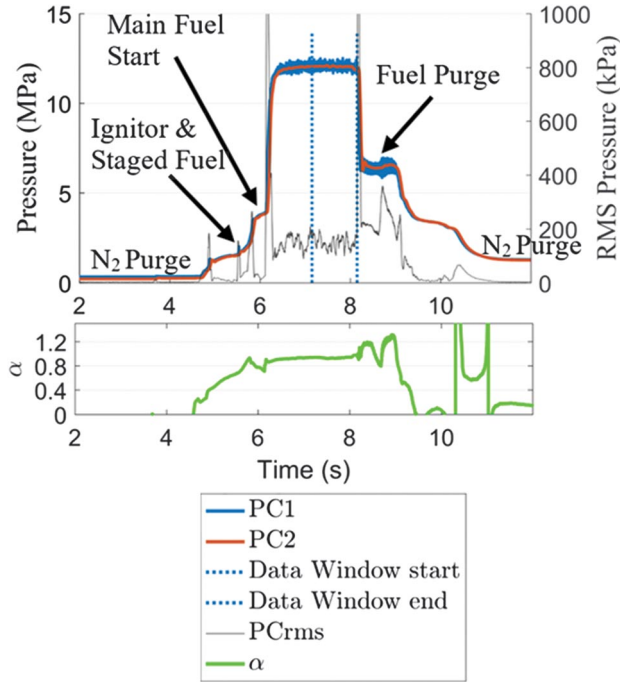


Fig. 10 Time histories of pressure and α for full test sequence at 12.4 MPa and mixture ratio of 3.2. Run 134.

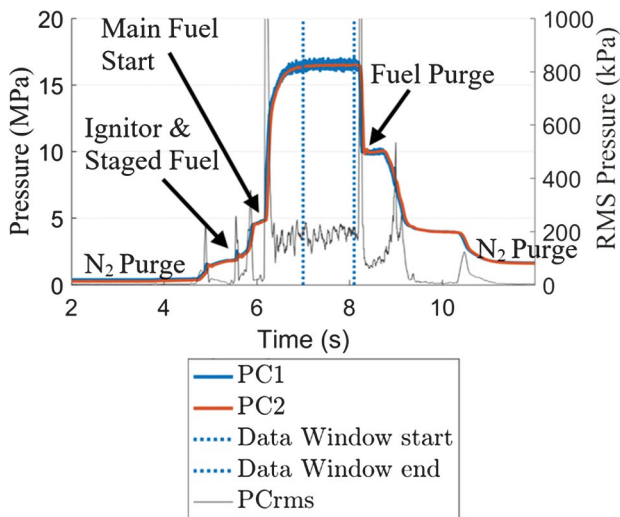


Fig. 11 Time histories of pressure for full test sequence at 16.5 MPa and mixture ratio of 2.86. Run 148.

shows the pressure traces for the main chamber, PC1 and PC2, as well as the calculated rms value of the fluctuating pressure component, P' , calculated from PC1. The dominant instability mode corresponded to a low-frequency longitudinal thermoacoustic instability at 200–250 Hz, well below the 500 Hz Nyquist frequency for PC1. The lower portion of Fig. 10 provides the time variation of a dimensionless GOX post temperature α , which is defined in the next section. The time coordinate is cropped to show only the 10 s segment of the test during which the combustor fires. Annotated on the figure are indicators for each stage of the test sequence, including bounds on the data window. Note that, during the higher-pressure tests, there is a relatively stable period between the start and end of the fuel purge, which corresponds to the lean period of data.

A. Flame Anchoring

The injector borescope and GOX post thermocouple provide insights into flame stability and the anchoring location within the injector cup. Using these two measurements, the presence of any

combustion upstream of the injector face can be verified for all stable test conditions. This is an important point because the side-viewing window does not enable measurement of the flame position relative to the GOX post upstream of the injector face. Some images also suggest that the flame begins downstream of the injector face. The borescope imaging clearly shows that this is due to blockage of flame luminosity by the spray and/or soot.

The temperature at the GOX post thermocouple position is a function of fuel temperature, oxidizer temperature, and conduction/radiation from the flame. To provide a consistent comparison across conditions of varying fuel and GOX inlet temperature, a nondimensional parameter α is defined in Eq. (3) as the ratio of the difference between the GOX post temperature and the fuel temperature to the difference between the GOX inlet temperature and the fuel temperature. Assuming a thermocouple accuracy of ± 2 K, the resultant absolute uncertainty in α is ± 0.015 :

$$\alpha = \frac{T_{\text{GOXPostTC}} - T_{\text{LHC}}}{T_{\text{GOXInlet}} - T_{\text{LHC}}} \quad (3)$$

In a nonreacting flow, α must satisfy the inequality $0 < \alpha < 1$ and can be interpreted as the relative heat transfer to the thermocouple tip from the oxidizer and fuel. A value of $\alpha = 1$ or 0 would correspond to the limit of only GOX or fuel flow, respectively. Because fuel temperature throughout all test campaigns remained relatively constant, changes in α must be attributable to changes in oxidizer temperature, relative fuel/oxidizer flow rates, or flame heat transfer. If the flame is thermally communicating with the GOX post, however, the post thermocouple's temperature can lie above that of the GOX, that is $\alpha > 1$. In this case, α is an indicator of the relative strength of heat transfer to the GOX post tip.

Figure 10 shows an example time series of α for an entire test run. Typically, the value of α reaches a quasi-steady value between 0.5 and 1.5 during the data window and exhibits spikes at transitions, such as sudden changes in propellant flow. To analyze various correlations of α , its average value α_{avg} was calculated over 200–600 ms intervals (depending upon the transient rate in the averaging window) of main chamber combustion over a given test and for a range of operating conditions, to yield a number of test points.

Figure 12 presents correlations of α_{avg} with the mixture ratio and P' , given as a percentage of the static chamber pressure, during the

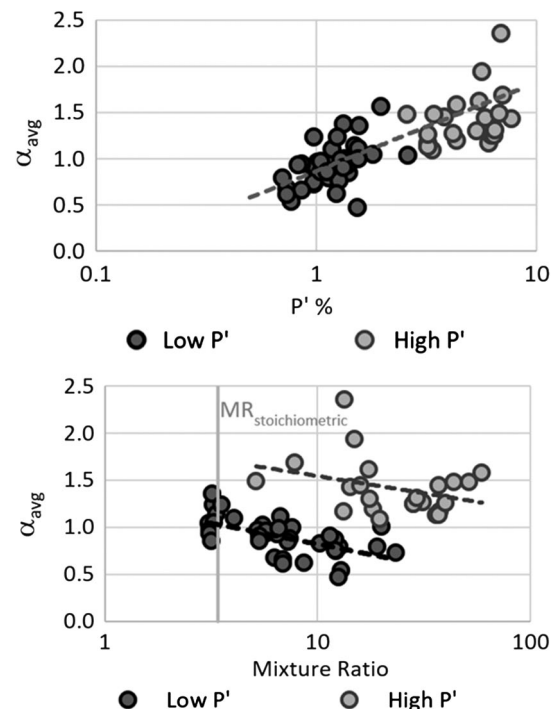


Fig. 12 Correlation of α_{avg} with P' and mixture ratio. Data representing runs 82–141.

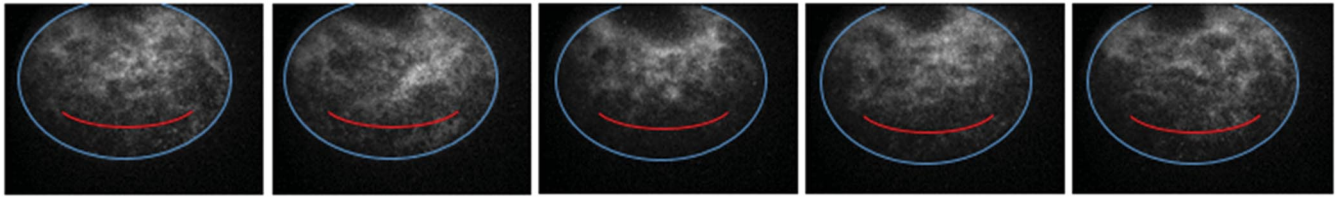


Fig. 13 Borescope view, instantaneous image series. Run 117, $P = 5.18$ MPa, $MR = 7.37$, $v_{LHC} = 6.63$ m/s.

corresponding time frame that α is averaged over. The data include steady-state conditions from all successful tests, often with multiple distinct steady states per test, with each data point representing a single steady-state condition. Starting with the pressure standard deviation plot, the data clearly show a monotonic rise in α_{avg} with pressure oscillation amplitude. Assuming that the flame is not in direct thermal contact with the GOX post (in other words, that it is stabilized some distance from the GOX post tip), this result is expected because larger-amplitude oscillations cause the flame to oscillate axially and spend more time in thermal contact with the GOX post. These same data are replotted as a function of the mixture ratio in the second plot. The data are color-coded by the results, where $P'/\bar{P} < 2.5\%$ is labeled low P' and $P'/\bar{P} > 2.5\%$ as high P' .

Consider next the MR correlations of GOX post temperature. These data clearly indicate that α_{avg} decreases with increasing mixture ratio, that is, with overall excess oxidizer. Given a constant GOX flow rate, mixture ratio is inversely proportional to fuel flow rate and, therefore, injection velocity. Although not shown, the data show α_{avg} to be uncorrelated with GOX flow rate and to linearly increase with fuel flow rate or velocity. Following the discussion of Eq. (1), this behavior is opposite of what would be observed in the nonreacting flow, as α_{avg} increases with increasing mixture ratio. This trend, along with the fact that α_{avg} achieves values greater than unity in some cases, strongly suggests that it is not a nonreacting heat transfer effect but rather a manifestation of a change in the flame's thermal interaction with the GOX post as MR increases. In particular, it suggests either that the flame is physically moving downstream, and thus reducing convective/conductive heat transfer to the GOX

post, or that the radiative heat transfer back to the GOX post is decreasing as MR increases. Either or both of these processes would be expected to occur, as the flame is leaning out.

B. Flame Structure near Injector Cup

This section presents borescope images of the flame from within the oxidizer flow. This location is advantageous because the soot cloud in nonpremixed flames is on the fuel side, and so it separates the flame from the windows in the combustor. In contrast, in viewing the flame from the oxidizer side, the soot emissions are far less problematic, even at globally rich conditions, eliminating the need for infrared diagnostics. This vantage point enabled the use of chemiluminescence imaging at high-pressure, rich conditions, to indicate the location of the reaction zone. Figure 13 presents several successive instantaneous images, taken at 430 fps with $10 \mu s$ exposure. The red line denotes the location of the inner edge of the injector cup bevel, and the blue line denotes the GOX post tip, as seen in Fig. 8b.

Comparing with the calibration image presented in Fig. 8, it is evident that combustion begins at the GOX post tip, where the fuel is first introduced. Luminosity at the post tip is relatively dim, and a gradual increase in intensity is seen as the flow leaves the injector. There is a significant, small-scale spatiotemporal variation in flame luminosity, presumably due to turbulent flame wrinkling.

Figure 14 shows a time-averaged image for the same run as the instantaneous images in Fig. 13. These images indicate a nominally axisymmetric luminosity distribution, with some evidence for weak nonaxisymmetric flame tendrils coming back to the GOX post tip. The locations of the fuel delivery orifices, from Fig. 8c, have been superimposed. No obvious correlation exists between the flame asymmetry and the locations of the fuel holes.

As the fuel flow rate and propellant velocity increase (at higher chamber pressures), a much more marked asymmetry in the fuel distribution appears. Figure 15 shows a sequence of borescope images, again captured at $10 \mu s$ exposure, indicating distinct spirals of luminosity. These spirals appear to be directly correlated with the swirling fuel exiting the individual fuel orifices. This can be more clearly seen in Fig. 16, which shows a time-averaged image for this same high-pressure, lower mixture ratio run, with the fuel orifices superimposed.

Experiments by Schmidt et al. have found similar, asymmetric liquid structures in rocket injector sprays using time-gated ballistic photon imaging [24]. These experiments noted a thin, organized pattern of liquid structures emanating from the injector, likely resulting from the nonuniform injection holes in the injector.

Such marked asymmetry is significant for two reasons. First, it shows that computations of this system must resolve the individual

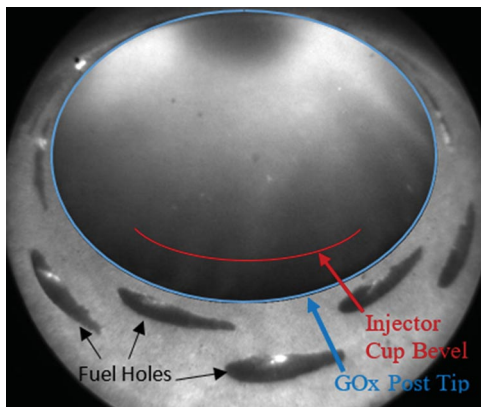


Fig. 14 Borescope view, time-averaged image, with calibration image (Fig. 6) overlay. Run 117, $P = 5.18$ MPa, $MR = 7.37$, $v_{LHC} = 6.63$ m/s.

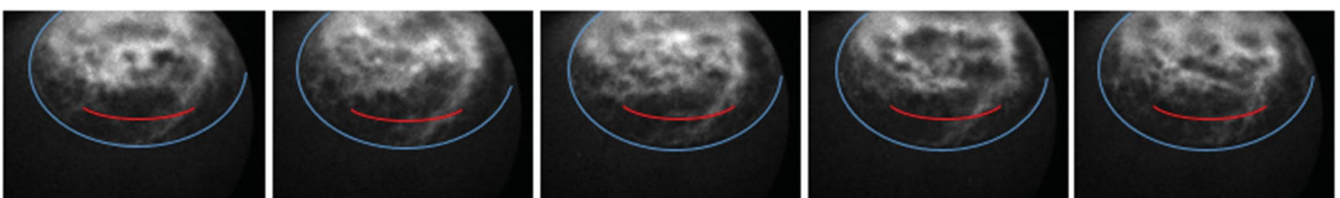


Fig. 15 Borescope view, instantaneous image series. Run 141, $P = 14.0$ MPa, $MR = 4$, $v_{LHC} = 64.3$ m/s.

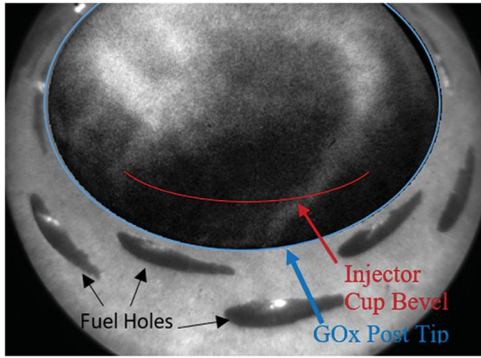


Fig. 16 Boreoscope view, time-averaged image, with calibration image (Fig. 6) overlay. Run 141 $P = 14.0$ MPa, $MR = 4$, $v_{LHC} = 64.3$ m/s.

fuel injection holes. Second, it shows a significant change in the flame structure at a higher pressure and flow velocity.

To convert these boreoscope images into quantitative values for further analysis, the weighted luminosity was measured as a function of downstream distance. Figure 8 shows the section of the boreoscope image where luminosity was evaluated. The white lines denote the endpoints of the arcs over which intensity was azimuthally integrated and then averaged over arc length for successive axial locations. Figure 17 plots this weighted luminosity with respect to axial position for a set of runs with varying mixture ratio and pressure. The overall observation from the figure is that luminosity grows with downstream distance before peaking and then dropping in the far field for all test cases.

It has previously been shown that α_{avg} decreases with increasing mixture ratio. Supposing that this effect is due to the translation of the flame downstream, some insight into this hypothesis can be obtained by looking at the relative CH^* luminosity near the GOX post tip for varying α and mixture ratio, as shown in Fig. 18. Luminosity was measured from a single pixel, providing a line-of-sight integrated measurement along a probe volume that ends at a location just downstream of the GOX post tip. This target location is 0.7 mm downstream of the GOX post tip, at the bottommost point along the circumference of the injector, visible within the boreoscope image. These comparisons show only a weak correlation of α or MR with luminosity. For low P' conditions, as defined previously, greater luminous intensity is associated with increasing α_{avg} and decreasing MR. No correlation is evident for high P' conditions. This suggests that, under low P' conditions, the flame moves downstream slightly

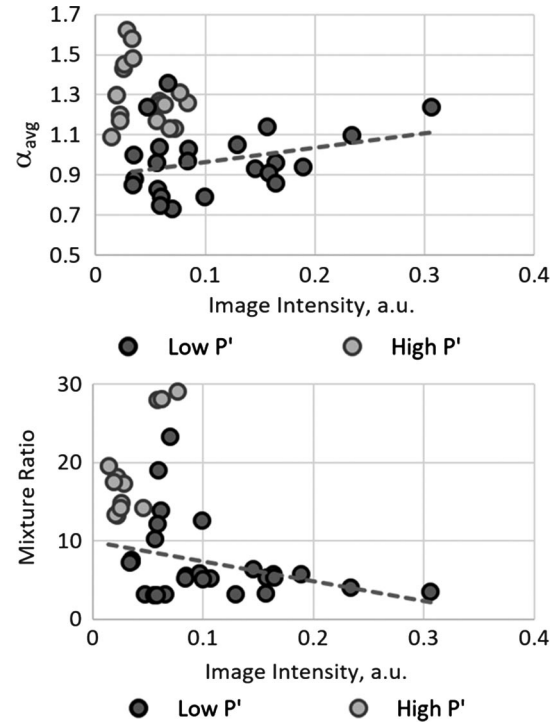


Fig. 18 Plot of α and MR with respect to boreoscope image intensity near GOX post tip. Data representing runs 82–141.

as the mixture ratio increases, resulting in less heat transfer to the GOX post tip.

Another item that can be observed in the latter set of conditions is the dark spot in the far field of Fig. 14. There is a noticeable reduction of intensity far from the injector post, suggesting the termination of combustion. This “dark spot” is also evident from Fig. 17, showing the negative slope, starting beyond ~ 3 cm axial distance from the post tip. For a nonpremixed flame with globally lean mixtures, it may be expected that the overventilated flame does not close around the jet of oxygen but rather spreads to the walls because of the more abundant, center oxygen stream. In contrast, the underventilated flame will close in on the center for a globally rich mixture, as depicted in Fig. 19.

The dark spot in the mixture ratio can be seen in Fig. 20, which shows boreoscope images from a transient condition as fuel flow rate is

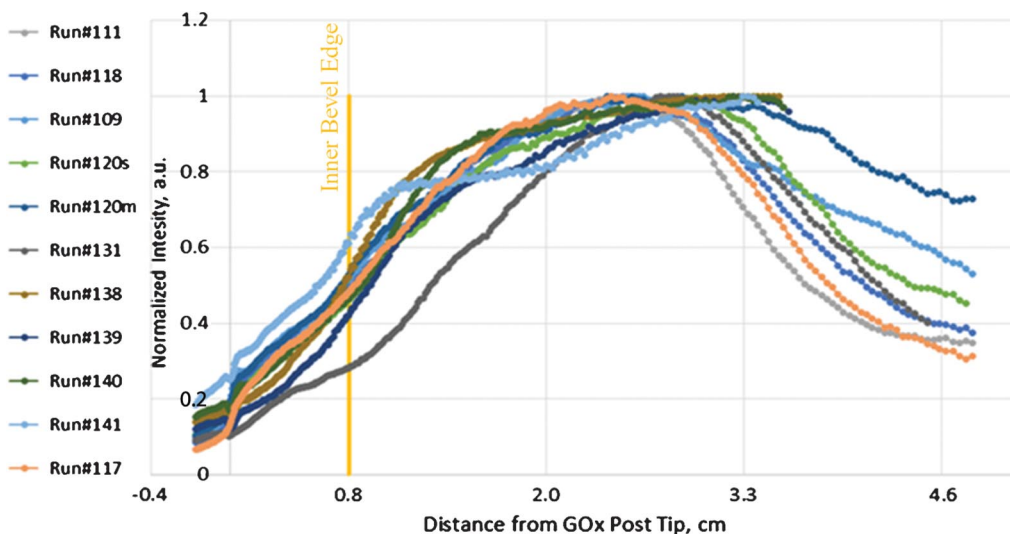


Fig. 17 Boreoscope normalized, weighted luminous intensity with respect to axial distance from GOX post.

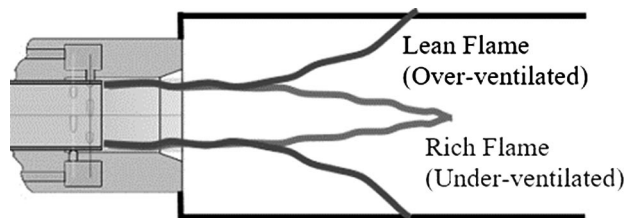


Fig. 19 Depiction of flame position for globally rich and lean conditions.

increased. The mixture ratio begins very lean in the leftmost image ($MR \cong 50$) and becomes more rich until a steady-state condition is achieved in the rightmost image ($MR = 5.5$). This progression corresponds to a contraction of the dark spot as the mixture ratio is decreased.

It can be anticipated that, for a nonpremixed flame, the size of the dark spot is a function of mixture ratio. The size of the dark spot was quantified by measuring the radius at 92% of maximum image intensity and measuring the center point luminosity at 3.68 cm from the GOX post. Figure 21 plots both the measured radius of the dark spot and center point luminous intensity with respect to the mixture ratio; both measurements are illustrated in Fig. 20. These images show that luminosity decreases in the far field with increasingly lean mixtures. Figure 17 also supports this observation, as intensity drops off farther from the injector, at the far right.

C. Flame Position

Optical access through the side windows allowed for qualitative and quantitative flame-shape analyses. As noted earlier, initial test campaigns used imaging of OH^* and CH^* species in the combustor. However, the first test campaign revealed that significant quantities of soot obscured the flame, making diagnostics in the visible and ultraviolet spectrum essentially useless at elevated pressures and lower mixture ratios. The visible and UV cameras captured clear images of ignition but rapidly became completely dark as the fuel flow rate and pressure increased.

Figure 22 shows a time series of CH^* and OH^* filtered high-speed camera images taken at low pressures and high MR, just after the main chamber ignition. The visible CH^* filtered image, in red, is overlaid with the UV OH^* filtered image, in green. Times from ignition and static pressure are provided at the bottom of the image. A model of the injector is overlaid to indicate the position of the injector in the frame.

From the limited chemiluminescence data, a comparison could be made between CH^* and OH^* species concentrations. There is a separation between the locations of these species in the flame, with the CH^* present earlier in the flame, whereas the OH^* appears downstream. The two regions overlap, but it is typically observed that OH^* is present farther downstream. This condition is not limited to ignition, as shown in the last image of Fig. 22, captured more than 100 ms after ignition. This is an interesting observation with two potential explanations. The first possible reason is that the OH^* is dominated by a thermal production mechanism, rather than chemiluminescence, and so indicates the presence of hot combustion products downstream of the region of

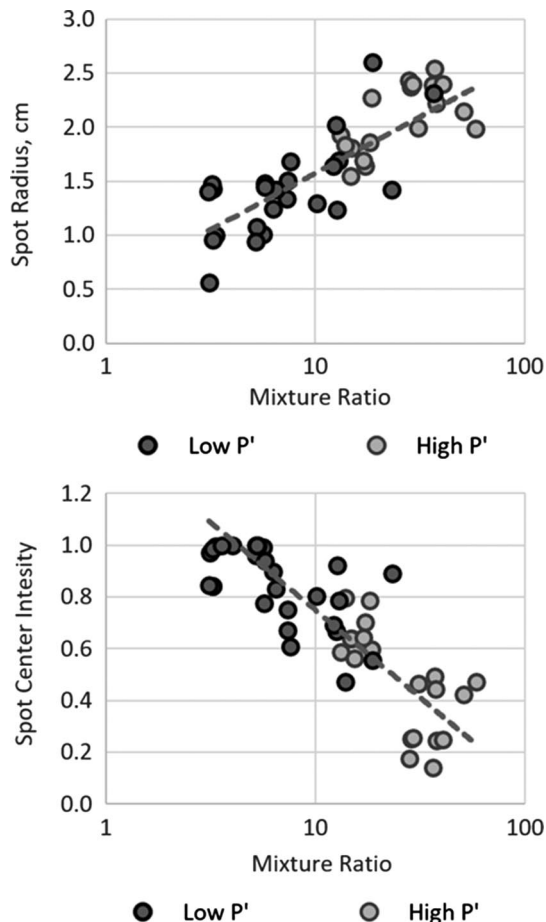


Fig. 21 Dark spot radius and normalized luminous intensity at center, with respect to MR. Runs 82–141.

chemical reaction, denoted by CH^* . Calculations by Nori suggest that thermal production of OH^* increases rapidly with pressure and temperature and can account for greater than 30% of the total production at only 1.52 MPa and 695 K, for residence times similar to those of this combustor [25]. Both temperature and pressure inside the chamber significantly exceed these reference values, such that even greater production of thermal OH^* should be expected, supporting the inference. The second possible reason is that OH^* and CH^* are indicators of reaction rates, but combustion occurs in two stages; for example, the fuel breaks down into H_2 and CO , with CO to CO_2 chemistry occurring near the injector and H_2 to H_2O chemistry dominating the region downstream.

Preliminary investigation of alternative optical diagnostics found high transmissivity for soot in the 3–5 μm wavelength infrared spectrum. Based on absorption/emission spectra of CO_2 and H_2O , two suitable wavelengths within this spectrum were identified for combustion imaging. Excited H_2O species emit at

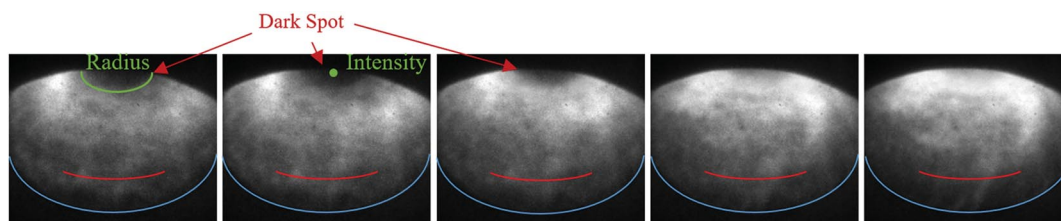


Fig. 20 Borescope view, time-averaged series showing transient. Left to right, MR decreases from ~ 50 to 5.5, pressure increases from 6.9 to 8.3 MPa. Run 12.

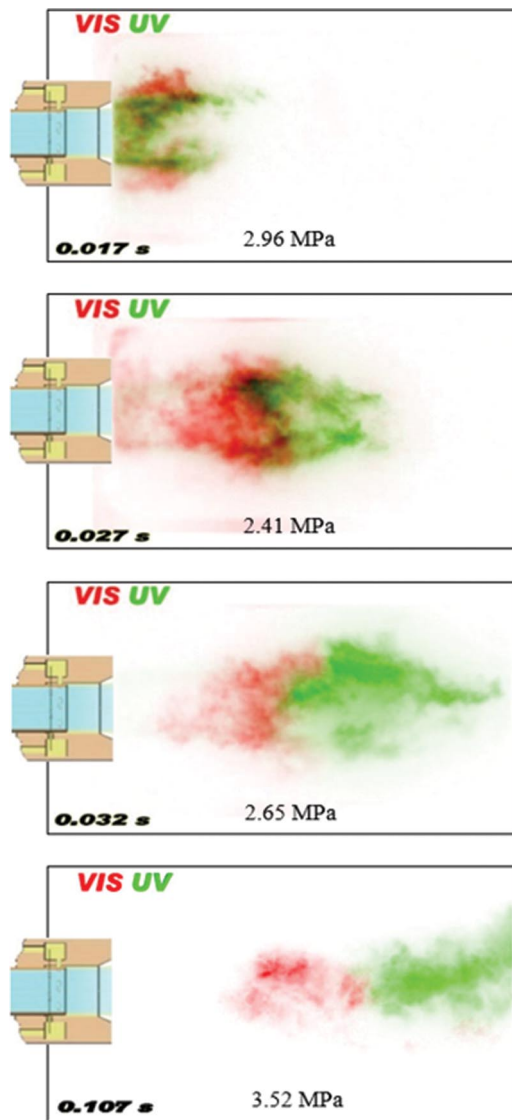


Fig. 22 Side-on view, instantaneous composite series of CH^* and OH^* images after ignition. Run 19.

2.8–3.5 μm , whereas CO_2 species emit at 4.25–4.75 μm [26]. Demonstration using an IR camera validated this method, producing clear images of an oxyacetylene flame through a visibly opaque, soot-covered window at both of the identified wavelengths. Based on the success of this test, an IR camera was procured for subsequent testing, replacing the UV camera used in the first tests.

During the second and third campaigns, the IR camera demonstrated significantly improved performance over the visible and UV. However, the IR images were still susceptible to liquid fuel deposition and thick soot clouds, particularly at high pressures. Although the infrared technique often provides useful data at the steady-state operational conditions, there are some high-pressure, low-mixture-ratio conditions that preclude even IR diagnostics. It is also important to note that the infrared bandwidths selected for this study do not correspond to chemiluminescence species or reflect heat release. Rather, the infrared images captured indicate hot H_2O and CO_2 that reflect the distribution of hot products in the combustor.

Figure 23 shows a time series of images from the IR camera, taken at a low-pressure, high mixture-ratio condition during the roughly steady-state portion of the purge period of the run. As in Fig. 22, a representation of the injector is depicted on the leftmost frame to indicate its position, and propellants travel left to right in the frame.

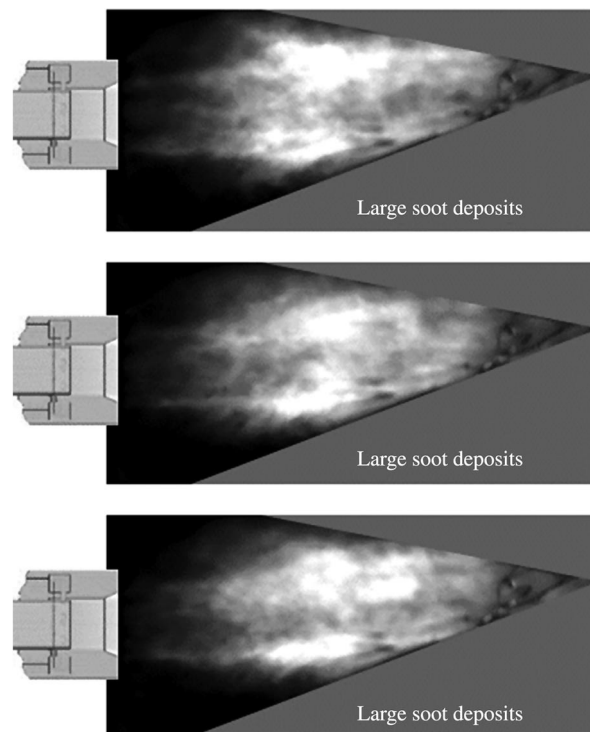


Fig. 23 Side-on view, instantaneous sequence of IR images. Run 105, $P = 3.79$ MPa MR = 11.46, wavelength = 2.75 μm .

Hot products can be observed issuing from the injector cup, forming a narrow spreading sheet. Farther downstream, the zone of luminosity broadens significantly, due to increased flame brush flapping and possibly also to recirculating flow. Note that there are soot deposits on the windows from a preceding richer condition, obscuring the view of the flame.

Anchoring of the flame upstream of the injector face can be inferred for this test condition, based on the borescope chemiluminescence measurements. Based on the side-on IR images, however, it is not generally possible to verify the flame anchoring. The absence of increased IR intensity at the injector face is attributable to soot in the recirculation zones and liquid fuel shrouding the jet. Thus, the side-on IR images do not demonstrate detachment from the injector. Rather, as discussed earlier, the GOX post thermocouple and borescope chemiluminescence images indicate the presence of the flame all the way back to the GOX post.

At higher- v_{LHC} , high-pressure cases, the images suggest that discrete fuel jets are entering the combustor. The jets can be seen by adjusting the gain and focusing on the very near-injector region. At high pressure and low MR, soot completely obscures the flame image, but the interior flame provides a backlight that scatters off the fuel spray, which can be seen through the soot. This perspective, similar to a shadowgraph image, reveals detail of the fuel spray and vaporization even at very high pressures, where the rest of the flame is not visible. Figure 24 shows a sample of near injector images, with progressively increasing fuel injection velocity. Image contrast and gain are increased by a factor of 4 from the left image to the right to compensate for increasing IR absorption by soot.

Consistent with the observations obtained from the borescope, no discrete fuel pattern is visible at the lowest fuel injection velocity. Very little soot is present in this image, and the flame is visible. The second image in Fig. 24 shows an increase in soot dispersing from the injector and, again, no discernible discrete fuel pattern. At conditions of very high fuel velocity, as in the right image of Fig. 24, four streaks of intensity can be seen entering the combustor.

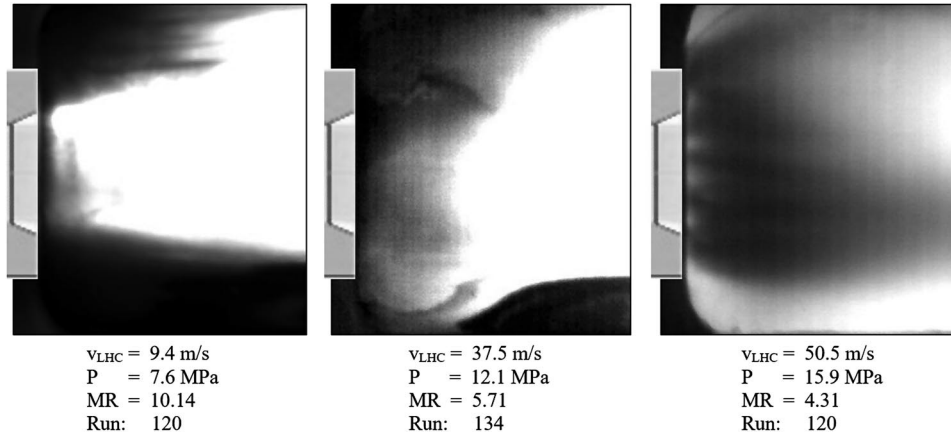
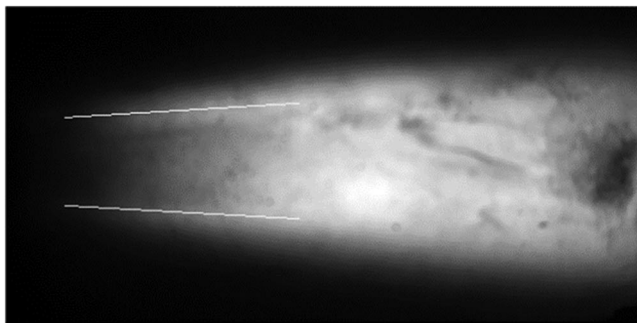


Fig. 24 Time-averaged IR images showing fuel spray from the injector at increasing pressure/fuel flow rate. Wavelength = $2.75 \mu\text{m}$.

For flame-shape analysis, a series of IR flame images from each test were time-averaged over a length of 50–100 ms. Averaging time was limited by the presence of large, moving soot structures, which could distort the compiled image over the length of the steady-state data window (approximately 1 s). As such, averaging time was chosen to avoid significant interference, if possible. Some of the IR data were recorded during the stable purge period of the test because the lower pressure and fuel flow rates result in lower soot. During the second test campaign, this reduced fuel flow rate was unmeasured, and there is no mixture ratio calculation for those data sets.

Flame spreading angles are approximated from time-averaged IR images. A filter is applied to the image to eliminate the large spatial structures. This is done by taking a two-dimensional Fourier transform of the time-averaged image, removing the low-wave-number content ($k_D < 5.5 \text{ cm}^{-1}$ horizontal, $k_D < 11 \text{ cm}^{-1}$ vertical), and then performing an inverse Fourier transform.



Spreading Angles: 3.48° , -3.23°
 Sample: 2.8 cm starting 0.7 cm from injector face

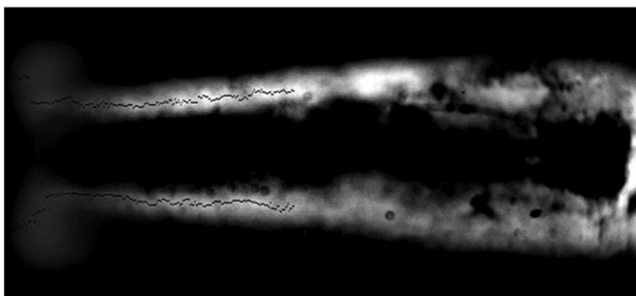


Fig. 25 Time-averaged IR image with measured spreading angle overlaid (top), and spatially high-pass-filtered result (bottom). Run 49, $P = 4.34 \text{ MPa}$.

Figure 25 exemplifies the result of this process, where the bottom image is the filtered result of the (top) original image. Within the frequency-filtered image, the location of maximum intensity for each axial location is identified, as depicted by black dots along the top and bottom bands in the bottom image of Fig. 25. A linear regression of these locations provides an approximation of the flame spreading angle, recorded in the text between the top and bottom images, along with the dimension of the measured section. The white lines overlaid on the original image represent the resulting fit to the maximum intensity points from the filtered image on bottom. The uncertainty in spreading angle is $\pm 0.5 \text{ deg}$.

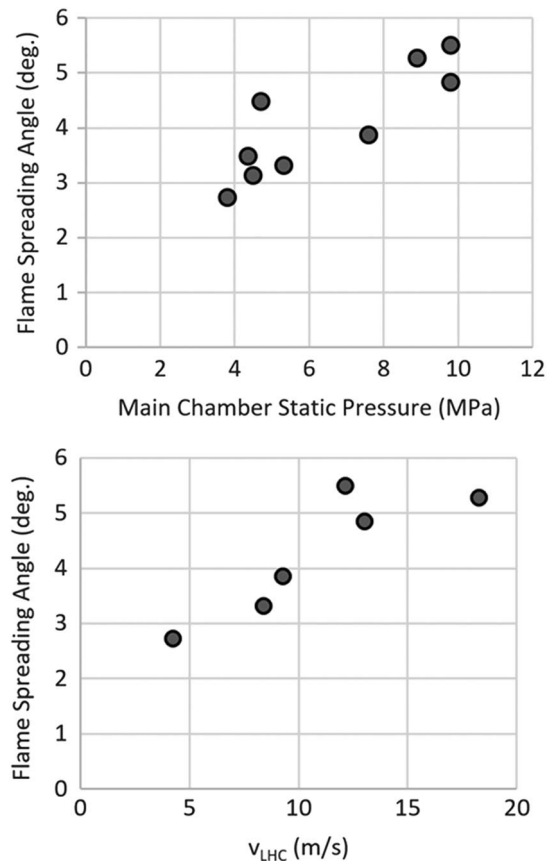


Fig. 26 Correlation of flame spreading angle with combustion pressure and v_{LHC} . Data include runs 49, 71, 75, 105, 120, 146, and 147 with MR between 5 and 18.

based on sensitivity to the wave-number threshold and variation in measurement location.

Figure 26 plots the estimated flame angle obtained from the top half of filtered images as a function of chamber pressure and reference fuel velocity, for mixture ratios of 5–30. This analysis was limited to low P' , lean conditions, when soot and fuel obscured less of the flame. The correlation is also limited to the top side angle because the bottom of the window accumulated significantly more soot. Figure 26 shows that the flame spreading angle increases with both chamber pressure and fuel velocity. Note that higher reference axial fuel velocities also equate to higher azimuthal velocities, which may explain the increased spreading angle with fuel velocity.

V. Conclusions

This paper presents results from a high-pressure optically accessible single injector gaseous oxygen (GOX)/liquid fuel test article. Key results from these studies are that, first, the flame remains close to the GOX post for all tested pressures and mixture ratios (MRs) (that is, the flame is not lifted). Nonetheless, pressure and MR clearly change the degree of thermal interaction of the flame with the GOX post. Temperature data from the integral injector thermocouple,

along with borescope images, show that proximity of the flame and heat transfer to the GOX post tip (the fuel/oxidizer mixing point) is positively correlated with the amplitude of standard deviation of pressure and negatively with mixture ratio. In addition, the structure of the flame near the GOX post clearly changes with pressure, evolving from nearly axisymmetric at low pressures, to a much less axisymmetric structure with helical, luminous spirals at high fuel velocities/chamber pressures. These images show that computations of the flame shape must resolve the individual fuel injection holes of a multi-orifice injector to capture the flame shape near the injector. Finally, side-on images show the flame spreading downstream at an angle between 3 and 6 deg increasing with pressure and reference fuel velocity.

The key challenge encountered in this work was side-on imaging, due to significant soot formation. This issue would be less problematic in fuel-centered configurations because the soot would not be formed between the flame and the viewing window. However, it does indicate the need for development of improved diagnostic techniques using either shorter or longer wavelength, to penetrate the soot cloud and window deposition.

Appendix A: Test Conditions

Table A1 List of main data window conditions referenced in paper

Run	Date	Data window averaged MC pressure, MPa	Data window averaged MR	GOX preburner outlet temperature, K	Reference fuel velocity v_{LHC} , m/s	Nitrogen cooling flow, % (total propellant)	High-speed cameras	Borescope
19	16 Aug.	4.86	3.62	691	13.30	5	Vis./UV	No
49	17 Nov.	4.36	3.36	281	15.12	N/A	Vis./IR	No
71	21 Nov.	5.69	6.95	634	7.42	N/A	Vis./IR	No
75	22 Nov.	5.33	5.79	681	8.42	N/A	Vis./IR	No
82	6 March	3.74	6.33	625	7.99	21	Vis./IR	Yes
83	6 March	3.98	6.86	632	7.37	28	Vis./IR	Yes
84	6 March	3.99	6.292	634	8.04	29	Vis./IR	Yes
87	7 March	1.25	20.8	645	2.42	18	Vis./IR	Yes
88	7 March	1.84	20.5	574	2.42	18	Vis./IR	Yes
91	8 March	3.13	12.07	588	4.11	30	Vis./IR	Yes
92	8 March	3.13	12.9	583	3.89	29	Vis./IR	Yes
95	9 March	1.76	12.42	599	4.00	45	Vis./IR	Yes
96	9 March	3.37	12.54	602	3.91	46	Vis./IR	Yes
97	9 March	3.79	12.5	573	3.91	46	Vis./IR	Yes
98	9 March	3.97	12.44	593	3.91	46	Vis./IR	Yes
99	9 March	4.96	3.185	626	15.32	42	Vis./IR	Yes
100	9 March	6.00	3.096	611	15.73	42	Vis./IR	Yes
103	10 March	5.21	3.121	572	15.67	41	Vis./IR	Yes
105	10 March	5.34	3.121	596	15.73	41	Vis./IR	Yes
109	14 March	5.52	3.123	585	15.90	41	Vis./IR	Yes
110	14 March	6.06	3.085	568	15.84	41	Vis./IR	Yes
111	14 March	4.96	7.539	554	6.47	39	Vis./IR	Yes
117	15 March	5.18	7.37	595	6.63	39	Vis./IR	Yes
118	15 March	5.10	7.262	623	6.66	40	Vis./IR	Yes
120	15 March	8.89	5.196	616	18.29	25	Vis./IR	Yes
123	16 March	6.33	12.232	587	7.81	31	Vis./IR	Yes
125	16 March	9.77	3.257	591	29.22	25	Vis./IR	Yes
126	16 March	8.38	12.635	590	17.70	16	Vis./IR	Yes
129	17 March	11.93	6.67	571	33.59	24	Vis./IR	Yes
130	17 March	11.80	6.429	612	33.69	26	Vis./IR	Yes
131	17 March	8.74	12.181	614	17.59	27	Vis./IR	Yes
134	20 March	12.13	5.717	645	37.88	21	Vis./IR	Yes
135	20 March	12.11	5.711	606	37.50	22	Vis./IR	Yes
138	22 March	12.66	5.293	634	41.20	23	Vis./IR	Yes
139	22 March	12.76	5.243	630	41.80	22	Vis./IR	Yes
140	22 March	13.49	4.043	617	54.16	21	Vis./IR	Yes
141	22 March	14.27	3.575	599	64.30	21	Vis./IR	Yes
142	22 March	13.79	3.427	439	66.94	22	Vis./IR	No
145	23 March	13.98	5.48	647	40.19	24	Vis./IR	No
146	23 March	15.87	4.309	649	50.46	24	Vis./IR	No
147	23 March	16.27	3.998	592	56.72	22	Vis./IR	No
148	23 March	16.55	2.87	619	79.33	22	Vis./IR	No

Table A2 List of secondary purge data window conditions referenced in paper

Run	Date	Secondary window averaged MC pressure, MPa	Secondary window averaged MR	GOX preburner outlet temperature, K	Reference fuel velocity v_{LHC} , m/s	Nitrogen cooling flow, % (total propellant)	High-speed cameras	Borescope
99	9 March	3.79	8.60	651	3.43	42	Vis./IR	Yes
99	9 March	3.56	5.13	644	5.75	42	Vis./IR	Yes
100	9 March	3.70	7.76	639	3.80	42	Vis./IR	Yes
103	10 March	3.78	11.39	553	2.60	41	Vis./IR	Yes
105	10 March	3.79	12.00	627	2.47	41	Vis./IR	Yes
109	14 March	3.89	18.14	633	1.66	41	Vis./IR	Yes
109	15 March	3.71	13.24	593	2.27	41	Vis./IR	Yes
110	14 March	3.92	19.60	621	1.51	42	Vis./IR	Yes
111	14 March	3.83	14.82	541	1.99	39	Vis./IR	Yes
111	14 March	3.70	13.36	546	2.21	39	Vis./IR	Yes
117	15 March	3.78	17.33	608	1.71	39	Vis./IR	Yes
117	15 March	3.67	14.25	615	2.08	39	Vis./IR	Yes
118	15 March	3.83	17.51	671	1.67	40	Vis./IR	Yes
120	15 March	7.53	10.22	637	5.63	25	Vis./IR	Yes
123	16 March	7.80	6.55	586	8.82	31	Vis./IR	Yes
124	16 March	5.70	13.88	387	4.17	29	Vis./IR	Yes
124	16 March	5.74	14.25	368	4.06	29	Vis./IR	Yes
125	16 March	4.63	36.96	616	1.56	25	Vis./IR	Yes
126	16 March	6.65	23.27	603	5.82	16	Vis./IR	Yes
129	17 March	7.93	19.89	539	6.82	24	Vis./IR	Yes
129	17 March	7.93	15.78	561	8.59	24	Vis./IR	Yes
130	17 March	7.91	19.02	621	6.89	26	Vis./IR	Yes
131	17 March	5.74	51.11	588	2.54	27	Vis./IR	Yes
131	17 March	5.73	58.87	580	2.20	27	Vis./IR	Yes
135	20 March	6.49	37.21	611	3.48	22	Vis./IR	Yes
135	20 March	6.49	31.07	614	4.17	22	Vis./IR	Yes
138	22 March	6.59	35.97	649	3.67	23	Vis./IR	Yes
138	22 March	6.70	28.00	649	4.71	23	Vis./IR	Yes
139	22 March	6.64	37.06	646	3.58	22	Vis./IR	Yes
139	22 March	6.69	28.15	649	4.71	22	Vis./IR	Yes
140	22 March	6.63	39.79	641	3.33	21	Vis./IR	Yes
140	22 March	6.69	29.07	644	4.56	21	Vis./IR	Yes
141	22 March	6.55	43.34	625	3.21	21	Vis./IR	Yes

Appendix B: Instrument Specification

Table B1 Diagnostics Employed during Experimental Campaigns

Data	Instruments	Quantity
<i>Test article</i>		
Chamber high-frequency pressure	HF/LF Kulite sensors, EWCTV-312-3000SG, 100 kHz	4
GOX chamber pressure	HF/LF Kulite sensors, EWCTV-312-3000SG, 100 kHz	1
LHC manifold pressure	HF PCB Piezotronics pressure sensor, 112A05, 100 kHz	1
Chamber low-frequency pressure	LF Taber pressure sensor, 2911, 1 kHz, 0.1% accuracy	2
Chamber metal temperature	K-type thermocouples, two depths, 1 kHz, $\pm 2^\circ\text{C}$	10
GOX post/injector tip temperature	Annular K-type thermocouple, 1 kHz, $\pm 2^\circ\text{C}$	1
<i>Cameras and optics</i>		
IR spectrum video	FLIR X6901sc InSb, 1700 FPS 640 × 512 resolution, $f/2.5$, CameraLink (CL) Full & CoaXPress (CXP), with ResearchIR Max #29267-201 and additional 100 mm lens, 3.0–5.0 μm	1
Visible spectrum video	Phantom 7000 FPS 768 × 400 resolution; Nikon 400 mm $f/2.8$ lens; HiCATT Intensifier, gain 600 V, gate 500 ns; CH filter (430 nm)	1
UV spectrum video	Phantom 7000 FPS 1008 × 504 resolution; Sodem 100 mm $f/2.8$ lens; HiCATT intensifier, gain 600 V, gate 500 ns; OH filter (308 nm)	1
Borescope	Gradient Lens Corp 7 in. Pro Slim Kit HI TEMP PS07-NVK-HI, diameter 4.2 mm; length 7 in.; angle of view 42 + 45 deg quartz prism (up to 300°C), 77 in. slim borescope, 90 deg mirror tube	1
Borescope intensifier	Generation III, bandwidth 350–900 μm (400–430 mm with CH* filter), phosphor P462 · 10 ⁻⁷ s decay time, active area diameter 18 mm, gate set: 10 μs , gain set: 10,000–20,000	1
Borescope camera	Basler acA1920–155 μm , sensor CMOS 2.3 Mpixel settings: 430 fps frame rate, 600 × 440 pixels, frame size exposure: 1000 μs	1
<i>Facility</i>		
Propellant inlet temperatures	K-type thermocouples, 1 kHz, $\pm 2^\circ\text{C}$	—
Propellant inlet pressures	Taber 2211 static pressure sensors, 1 kHz, 0.1% accuracy [23]	—
Gaseous flow rates	Critical flow nozzles, with density calculation based on preceding temperature/pressure instrumentation. Uncertainty: oxygen 0.5%, nitrogen < 10%	—
LHC flow rates	Primary: cavitating orifice with density calculation as before, uncertainty 0.4–0.5%. Secondary: positive displacement spur gear flow meter, AW Gear Meters JVM-20 KG-25-NPT, 0.5% uncertainty.	—

Acknowledgment

This work is partially supported by the David Lewis and William R. T. Oakes Endowments of Georgia Institute of Technology.

References

- [1] Harrje, D. T., and Reardon, F. H., "Liquid Propellant Rocket Combustion Instability," NASA SP-194, 1972.
- [2] Yang, V., and Anderson, W., *Liquid Rocket Engine Combustion Instability*, AIAA, Washington, D.C., 1995, pp. 3–38. doi:10.2514/4.866371
- [3] Lieuwen, T. C., *Unsteady Combustor Physics*, Cambridge Univ. Press, Cambridge, 2012, pp. XIII–XIX. doi:10.1017/CBO9781139059961
- [4] Candel, S., Herding, G., Synder, P., Scoufflaire, P., Rolon, C., Vingert, L., Habiballah, M., Grisch, F., Péalat, M., Douchardy, P., et al., "Experimental Investigation of Shear Coaxial Cryogenic Jet Flames," *Journal of Propulsion and Power*, Vol. 14, No. 5, 1998, pp. 826–834. doi:10.2514/2.5346
- [5] Mayer, W., and Tamura, H., "Propellant Injection in a Liquid Oxygen/Gaseous Hydrogen Rocket Engine," *Journal of Propulsion and Power*, Vol. 12, No. 6, 1996, pp. 1137–1147. doi:10.2514/3.24154
- [6] Santoro, R., Pal, S., Woodward, R., and Schaaf, L., "Rocket Testing at University Facilities," *39th Aerospace Sciences Meeting and Exhibit*, AIAA Paper 2001-0748, 2001. doi:10.2514/6.2001-748
- [7] Yeralan, S., Pal, S., and Santoro, R. J., "Experimental Study of Major Species and Temperature Profiles of Liquid Oxygen/Gaseous Hydrogen Rocket Combustion," *Journal of Propulsion and Power*, Vol. 17, No. 4, 2001, pp. 788–793. doi:10.2514/2.5834
- [8] Smith, J., Schneider, G., Suslov, D., Oschwald, M., and Haidn, O., "Steady-State High Pressure LO_x/H_2 Rocket Engine Combustion," *Aerospace Science and Technology*, Vol. 11, No. 1, 2007, pp. 39–47. doi:10.1016/j.ast.2006.08.007
- [9] Klimenko, D. N., Clauss, W., Oschwald, M., Smith, J., and Mayer, W., "CARS Temperature Mapping in a Cryogenic $\text{LO}_x\text{-H}_2$ Rocket Combustion Chamber Under Supercritical Conditions," *Journal of Raman Spectroscopy*, Vol. 33, Nos. 11–12, 2002, pp. 900–905. doi:10.1002/(ISSN)1097-4555
- [10] Hardi, J. S., Martinez, H. C. G., Oschwald, M., and Dally, B. B., "LOx Jet Atomization Under Transverse Acoustic Oscillations," *Journal of Propulsion and Power*, Vol. 30, No. 2, 2014, pp. 337–349. doi:10.2514/1.B34979
- [11] Richecoeur, F., Ducruix, S., Scoufflaire, P., and Candel, S., "Experimental Investigation of High-Frequency Combustion Instabilities in Liquid Rocket Engine," *Acta Astronautica*, Vol. 62, No. 1, 2008, pp. 18–27. doi:10.1016/j.actaastro.2006.12.034
- [12] Mery, Y., Hakim, L., Scoufflaire, P., Vingert, L., Ducruix, S., and Candel, S., "Experimental Investigation of Cryogenic Flame Dynamics under Transverse Acoustic Modulations," *Comptes Rendus Mécanique*, Vol. 341, Nos. 1–2, 2013, pp. 100–109. doi:10.1016/j.crme.2012.10.013
- [13] Yu, Y. C., Sisco, J. C., Rosen, S., Madhav, A., and Anderson, W. E., "Spontaneous Longitudinal Combustion Instability in a Continuously Variable Resonance Combustor," *Journal of Propulsion and Power*, Vol. 28, No. 5, 2012, pp. 876–887. doi:10.2514/1.B34308
- [14] Frezzotti, M. L., Terracciano, A., Nasuti, F., Hester, S., and Anderson, W. E., "Low-Order Model Studies of Combustion Instabilities in a DVRC Combustor," *50th AIAA/ASME/SAE/ASEE Joint Propulsion Conference*, AIAA Paper 2014-3485, 2014. doi:10.2514/6.2014-3485
- [15] Pomeroy, B., and Anderson, W., "Transverse Instability Studies in a Subscale Chamber," *Journal of Propulsion and Power*, Vol. 32, No. 4, 2016, pp. 939–947. doi:10.2514/1.B35763
- [16] Roa, M., Schumaker, S. A., Talley, D. G., and Bennewitz, J., "A Study of Acoustic Forcing on Gas-Centered Swirl-Coaxial Reacting Flows," *55th AIAA Aerospace Sciences Meeting*, AIAA Paper 2017-1335, 2017. doi:10.2514/6.2017-1335
- [17] Rankin, B. A., Blunck, D. L., Katta, V. R., Stouffer, S. D., and Gore, J. P., "Experimental and Computational Infrared Imaging of Bluff Body Stabilized Laminar Diffusion Flames," *Combustion and Flame*, Vol. 159, No. 9, 2012, pp. 2841–2843. doi:10.1016/j.combustflame.2012.03.022
- [18] Strakey, P. A., Talley, D. G., and Hutt, J. J., "Mixing Characteristics of Coaxial Injectors at High Gas/Liquid Momentum Ratios," *Journal of Propulsion and Power*, Vol. 17, No. 2, 2001, pp. 402–410. doi:10.2514/2.5756
- [19] Dranovsky, M. L., Yang, V., Culick, F., and Talley, D. G., *Combustion Instabilities in Liquid Rocket Engines: Testing and Development Practices in Russia*, AIAA, Reston, VA, 2007, pp. 242–282. doi:10.2514/4.866906
- [20] Trask, N., Schmidt, D. P., Lightfoot, M., and Danczyk, S., "Compressible Modeling of the Internal Two-Phase Flow in a Gas-Centered Swirl Coaxial Fuel Injector," *Journal of Propulsion and Power*, Vol. 28, No. 4, 2012, pp. 685–693. doi:10.2514/1.B34102
- [21] Wang, X., Li, Y., Wang, Y., and Yang, V., "Near-Field Flame Dynamics of Liquid Oxygen/Kerosene Bi-Swirl Injectors at Supercritical Conditions," *Combustion and Flame*, Vol. 190, April 2018, pp. 1–11. doi:10.1016/j.combustflame.2017.11.007
- [22] Austin, B. L. J., Schumaker, S. A., and Danczyk, S., "Laboratory-Scale Preburner for Selectable Flow Conditions in ORSC Experiments," *53rd AIAA/SAE/ASEE Joint Propulsion Conference*, AIAA Paper 2017-5012, 2017. doi:10.2514/6.2017-5012
- [23] Lightfoot, M. D., Danczyk, S. A., Watts, J. M., and Schumaker, S. A., "Accuracy and Best Practices for Small-Scale Rocket Engine Testing," *JANNAF 2011 Joint Subcommittee Meeting*, Air Force Research Lab Edwards AFB California Propulsion Directorate, AFRL-RZ-ED-TP-2011-420, Huntsville, AL, 2011.
- [24] Schmidt, J. B., Schaefer, Z., Meyer, T., Roy, S., Danczyk, S., and Gord, J., "Ultrafast Time-Gated Ballistic-Photon Imaging and Shadowgraphy in Optically Dense Rocket Sprays," *Applied Optics*, Vol. 48, No. 4, 2009, pp. B137–B144. doi:10.1364/AO.48.00B137
- [25] Nori, V. N., "Modeling and Analysis of Chemiluminescence Sensing for Syngas, Methane and Jet—A Combustion," Ph.D. Thesis, Georgia Inst. of Technology, Atlanta, GA, 2008.
- [26] Stein, S. E., *NIST Chemistry WebBook, NIST Standard Reference Database Number 69*, National Inst. of Standards and Technology, Mass Spectrometry Data Center, Gaithersburg, MD.

C. Segal
Associate Editor